Single-molecule orientation localization microscopy for resolving structural heterogeneities within amyloid fibrils

Tianben Ding,† Tingting Wu,† Hesam Mazidi, Oumeng Zhang, and Matthew D. Lew*
Department of Electrical and Systems Engineering,
Washington University in St. Louis, Missouri 63130, USA

Simultaneous measurements of single-molecule positions and orientations provide critical insight into a variety of biological and chemical processes. Various engineered point spread functions (PSFs) have been introduced for measuring the orientation and rotational diffusion of dipole-like emitters, but the widely used Cramér-Rao bound only evaluates performance for one specific orientation at a time. Here, we report a performance metric, termed variance upper bound (VUB), that yields a global maximum CRB for all possible molecular orientations, thereby enabling the measurement performance of any PSF to be computed efficiently (~1000 times faster than calculating average CRB). Our VUB reveals that the simple polarized standard PSF provides robust and precise orientation measurements if emitters are near a refractive index interface. Using the polarized PSF, we measure the orientations and positions of Nile red (NR) molecules transiently bound to amyloid aggregates. Our super-resolved images reveal the main binding mode of NR to amyloid fibers, as well as structural heterogeneities within amyloid fibrillar networks, that cannot be resolved by single-molecule localization alone.

INTRODUCTION

A key strength of single-molecule localization microscopy (SMLM) is its ability to measure the full distribution of the phenomena under study and avoid ensemble averaging. Going beyond standard SMLM to measure SM position and orientation simultaneously is critical for understanding a variety of nanoscale biological and chemical processes, such as the motions of molecular motors [1–3], the complex higher-order structures of DNA [4, 5], and reaction kinetics within catalytic nanoparticles [6]. To perform these measurements, molecular position and orientation must be encoded within the shape of the image produced by a microscope, i.e., its point-spread function (PSF). However, balancing the need to resolve various orientations unambiguously with the need to detect SMs efficiently with high signal-to-background ratio (SBR) remains a challenge that limits the adoption of Single-Molecule Orientation Localization Microscopy (SMOLM) for biological and chemical applications; existing techniques either cannot discriminate between similar types of molecular motions or cannot detect weak fluorescent emitters.

In order to design a PSF for measuring molecular orientation, one must have a figure of merit for comparison. The Cramér-Rao bound (CRB), which is the best-possible precision achievable by an unbiased estimator, has been used extensively for evaluating [7] and optimizing [8, 9] SMLM techniques. However, since CRB quantifies measurement performance locally, in the sense that it yields an expected measurement sensitivity for one specific molecular orientation, it is computationally expensive to characterize or optimize a PSF for all possible molecular orientations. Moreover, calculating this best-possible precision assumes that a single molecule has been detected, which may not be the case for low SBR conditions or when emitters are dense. We seek to develop an analytical framework for 1) quantifying the performance of any proposed method for measuring molecular orientation, 2) illuminating why a particular method performs well or poorly in a particular situation, and 3) comparing the sensitivity of various methods for measuring specific types of rotational motions.

In this paper, we derive a performance metric, termed variance upper bound (VUB), that globally bounds the CRB to quickly evaluate any optical method for measuring molecular orientation. Our VUB analysis surprisingly shows that a microscope with two polarization detection channels, exhibiting a polarized (standard) PSF, provides superior measurement precision when molecules are near a refractive index interface, especially when they lie perpendicular to the optical axis, even under low SBR. This conventional method of measuring molecular orientation has poor performance in index-matched samples unless a perturbation, such as defocus, is added to the optical system [10]. To demonstrate, we use a form of SMLM termed transient amyloid binding (TAB) [11] and a maximum likelihood estimator that promotes sparsity [12, 13] to measure the position and orientation of fluorescent molecules transiently bound to amyloid fibrils. For the first time to our knowledge, SMOLM reveals the orientation and rotational diffusion of Nile red (NR), a fluorescent molecule whose quantum yield increases when exposed to a nonpolar environment [14, 15], when bound to fibrils at the single-molecule level. We show that SMOLM probes structural heterogeneities within these amyloid aggregates that are not detectable by standard SMLM.

ORIENTATION LOCALIZATION MICROSCOPY AND VARIANCE UPPER BOUND

To begin, we model a fluorescent molecule as a dipole-like emitter [16] with an orientational unit vector $\boldsymbol{\mu} = [\mu_x, \mu_y, \mu_z]^T$, or equivalent angles (θ, ϕ) in spherical coordinates (Fig. S1). Assuming that a molecule's rotational correlation time is faster than its excited state lifetime and the camera integration time, its orientation trajectory can be modeled by a second-moment vector $\boldsymbol{m} = \left[\langle\mu_x^2\rangle, \langle\mu_y^2\rangle, \langle\mu_z^2\rangle, \langle\mu_x\mu_y\rangle, \langle\mu_x\mu_z\rangle, \langle\mu_y\mu_z\rangle\right]^T$, where each entry is a time-averaged second moment of $\boldsymbol{\mu}$ [17, 18]. These orientational second moments contain information on both the orientation of a molecule and its "wobble" or rotational diffusion, represented by Ω in solid angle, within a camera frame. Fluorescence photons collected from such an emitter are projected to a microscope's image plane with an n-pixel intensity distribution that can be modeled as a linear superposition of six basis images weighted by $\boldsymbol{m}$, i.e.,

$$\boldsymbol{I} = s\boldsymbol{B}\boldsymbol{m} + \boldsymbol{b} \in \mathbb{R}^{n\times 1} \tag{1}$$

$$= s\left[\boldsymbol{B}_{xx}\ \ \boldsymbol{B}_{yy}\ \ \boldsymbol{B}_{zz}\ \ \boldsymbol{B}_{xy}\ \ \boldsymbol{B}_{xz}\ \ \boldsymbol{B}_{yz}\right]\boldsymbol{m} + \boldsymbol{b}, \tag{2}$$

where s is the number of photons collected by the detector and $\boldsymbol{b}$ is the number of background photons in each pixel. Each so-called basis image $\boldsymbol{B}_j \in \mathbb{R}^{n\times 1}$, corresponding to the response of the optical system to each orientational second-moment component m_j, can be calculated by vectorial diffraction theory [17–20], and various optical elements, such as phase masks, polarizers, and waveplates, can be used to encode orientation information within $\boldsymbol{B}_j$ more efficiently. A key feature of this forward imaging model is its linearity with respect to the orientation parameters $\boldsymbol{m}$ of interest; $\boldsymbol{B}$ is simply a linear operator or transformation from object space to image space, and the fundamental measurement sensitivity of the optical system is bounded by considering $\boldsymbol{B}$ directly.

We next quantify the Fisher information (FI) contained in the basis images, i.e., the amount of information that the basis images contain about each of the orientational second moments. A larger FI corresponds to a smaller CRB and higher sensitivity for measuring $\boldsymbol{m}$. Given our linear imaging model, the FI matrix $\boldsymbol{J} \in \mathbb{R}^{6\times 6}$ for the orientational second moments can be written as (Supplementary Material 1A)

$$\boldsymbol{J} = \sum_{i=1}^{n} \frac{s^2}{I_i}\boldsymbol{B}_i^T\boldsymbol{B}_i = \boldsymbol{A}^T\boldsymbol{A}. \tag{3}$$

where $\boldsymbol{B}_i \in \mathbb{R}^{1\times 6}$ is the ith row of $\boldsymbol{B}$. Here, we introduce $\boldsymbol{A} \in \mathbb{R}^{n\times 6}$, where each entry of $\boldsymbol{A}$ can be bounded by (Supplementary Material 1A):

$$|A_{ij}| = \left|\frac{sB_{ij}}{\sqrt{s\boldsymbol{B}_i\boldsymbol{m} + b_i}}\right| \geq \left|\frac{sB_{ij}}{\sqrt{s\,\|\boldsymbol{B}_i\| + b_i}}\right| = \left|\hat{A}_{ij}\right|, \tag{4}$$

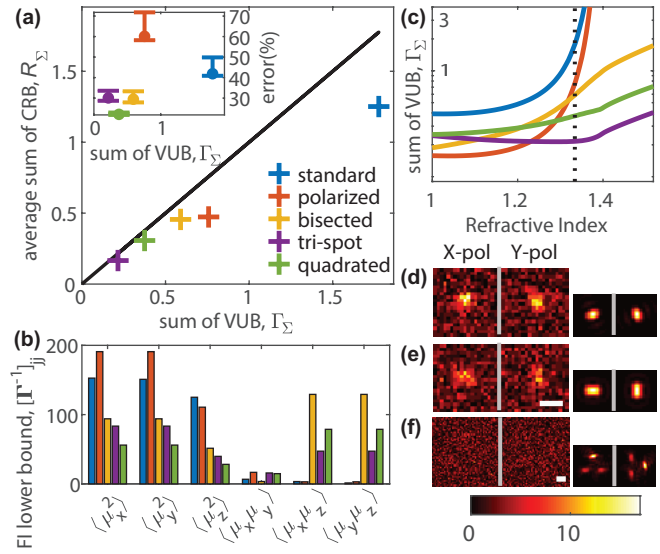

FIG. 1. Orientation measurement precision using various point spread functions (PSFs) for 380 signal photons and 2 background photons per pixel. (a) Average (over orientation space) sum R_Σ of the CRB over the six orientational second moments $\boldsymbol{m}$, versus the sum Γ_Σ of our variance upper bound (VUB) for various PSFs. Blue: (unpolarized) standard, red: polarized (standard), yellow: bisected, purple: tri-spot, and green: quadrated PSF. Dark line: Γ_Σ = mean of R_Σ. Inset: error of Γ_Σ relative to average R_Σ. Bars indicate minimum/maximum error relative to the mean (circle) over all of orientation space. (b) Fisher information (FI) lower bound $\left[\boldsymbol{\Gamma}^{-1}\right]_{jj}$ of each orientational second moment m_j. (c) Sum of VUB Γ_Σ for various refractive indices. Dotted line: refractive index of water. Simulated orthogonally polarized images of (d) a fixed molecule with orientation ($\theta = 90°$, $\phi = 45°$) and an isotropic emitter using (e) the polarized PSF and (f) the tri-spot PSF. Insets: normalized noiseless PSF images. Scale bars: 400 nm.

Since photon detection is a Poisson process, the entry A_{ij} represents the square root of the expected signal-to-noise ratio of the jth orientational second moment measured by the ith camera pixel.

Note that $\boldsymbol{J}$ is a function of $\boldsymbol{m}$ and may vary dramatically for different molecular orientations. We now develop our VUB matrix $\boldsymbol{\Gamma}$ (Supplementary Material 1A) to bound the CRB matrix $\boldsymbol{R} = \boldsymbol{J}^{-1}$ as,

$$\Gamma_{jj} = \left[\left(\hat{\boldsymbol{A}}^T\hat{\boldsymbol{A}}\right)^{-1}\right]_{jj} \geq \left[\boldsymbol{J}^{-1}\right]_{jj} = R_{jj}, \tag{5}$$

where the subscript jj denotes the jth diagonal element. Since $\boldsymbol{\Gamma}$ is independent of $\boldsymbol{m}$, i.e., it is only a function of the imaging system and not of a particular molecular orientation, VUB can be used to efficiently estimate the global performance of the imaging system and the precision of measuring each orientational second moment under various SBRs without expensive calculations of CRB.

We calculated the sum Γ_Σ of diagonal elements Γ_{jj} as

a summary measure of performance of five orientation-sensing PSFs, namely unpolarized standard, polarized standard, bisected [21], tri-spot [22] and quadrated [23], for a molecule emitting at a glass-water interface (Fig. 1(a)). To quantify the accuracy of our VUB, we compared Γ_Σ to the minimum/average/maximum value of the sum R_Σ of all diagonal entries of the CRB matrix over all of orientation space (Fig. 1(a) inset). We find Γ_Σ estimates the average R_Σ with an average error of 36% across the five PSFs. Note that computing Γ_Σ is faster than calculating the average CRB over all of orientation space (2500 sampling points) by a factor of ~1000. While the polarized standard PSF doesn't show the best variance Γ_Σ, its FI (in terms of $\left[\boldsymbol{\Gamma}^{-1}\right]_{jj}$) is large for the first four second moments (Fig. 1(b)), implying its superior sensitivity to these rotational motions. Therefore, the polarized PSF can estimate the in-plane (xy) orientations of fluorescent molecules with excellent precision (Fig. S2).

To explore the effect of refractive index (RI) mismatch, we evaluated Γ_Σ for sample media ranging from air (RI=1) to oil (RI=1.518). When RI is below 1.25, the polarized standard PSF surprisingly is the best PSF for 3D orientation measurements, followed by the tri-spot (Fig. 1(c)). This insight is confirmed by our observations that a molecule at an air-glass interface produces basis images $\boldsymbol{B}_j$ with vastly superior contrast (energy) compared to one within matched media (Fig. S3). On the other hand, for samples with RI near that of oil, PSF engineering clearly provides increased orientation precision over other approaches.

In addition to high orientation measurement precision, PSFs must be easily detectable under low SBRs in order to be practical for SMOLM. Using the polarized standard PSF, a fixed molecule ($\theta = 90°, \phi = 45°$) and an isotropic emitter can be easily distinguished from one another with only 380 photons detected (Fig. 1(d,e)). Note that distinguishing these two types of emitters is nearly impossible under matched RI conditions; it is the RI mismatch that enables this remarkable sensitivity. However, the tri-spot PSF, despite its superior VUB, cannot detect the same isotropic emitter due to the splitting of photons into three spots in each polarization channel (Fig. 1(f)). These observations suggest that the polarized standard PSF should be practical for measuring the positions and orientations of single fluorescent molecules precisely and sensitively.

RESOLVING STRUCTURAL HETEROGENEITIES WITHIN AMYLOID FIBERS

Amyloid aggregates are signatures of various neurodegenerative disorders such as Alzheimer's and Parkinson's diseases, and small soluble oligomeric intermediates formed during amyloid fibrillation are typically associated with cytotoxicity [24, 25]. Although many amyloid aggregates share a common cross-β sheet structural motif that is an assembly of identical copies of amyloid peptides, oligomers and fibrils are highly heterogeneous in terms of their structure and size [26, 27]. Interestingly, not all aggregation intermediates are equally toxic [28]. Here, we explore using SMOLM with the polarized standard PSF and Nile red (NR) for detecting the structural heterogeneity of amyloid fibrils. NR has been used as a surface hydrophobicity sensor for individual protein aggregates by measuring its emission wavelength while transiently and spontaneously bound to fibrils and protofibrils [29]. In this paper, we characterize NR's binding orientation as a method of mapping the organization of β-sheets within amyloid aggregates.

We prepared fibrils of amyloid-β peptide (Aβ42) adhered to cleaned glass-bottom imaging chambers as described previously [11] (Supplementary Material 2A). By adding 50 nM NR and illuminating with a 561-nm laser, we captured isolated fluorescence bursts corresponding to individual NR molecules transiently bound to the amyloid aggregates [11, 29] (Movie S1). The brightness (s), 2D position (x, y) and second-moment vector ($\boldsymbol{m}$) of individual NRs within each frame were jointly estimated by using a sparsity-promoting maximum-likelihood estimator [12, 13] followed by a weighted least-square estimator for projecting the estimated second moments to angular coordinates (ϕ, θ, Ω, Supplementary Material 2D).

The concentrated photon distribution of the polarized PSF enables our estimator to detect relatively dim molecules, providing > 1.4 localizations/nm on amyloid aggregates over ~3 min measurement time (Table S1). Fig. 2(a) shows a super-resolved fibril network. We estimate our localization precision to be 9 nm (std. dev., Fig. S4, Table S1). NR molecules exhibit strikingly different polarized PSFs depending on the long axis of the underlying fibrils (Fig. S10). Our orientation measurements show mostly in-plane polar angles ($\theta \approx 90°$, Fig. S11) and azimuthal orientations (ϕ) aligned to the long axis of amyloid fibrils (Figs. 2(b)-2(f)). These observations confirm that NR molecules preferentially bind to surfaces of β-sheets with their transition dipoles parallel to the fibril backbones (Fig. 2(b) inset), similar to the binding behavior of Thioflavin T [30, 31]. NR may bind transiently to grooves formed by adjacent amino acid side chains [32].

Although we observed most NR orientations to be parallel to the fibril backbones, these orientations are not always aligned with one another, even in neighboring structures. For example, two small aggregation limbs shown in Fig. 2(g) exhibit substantial differences in the standard deviation of azimuthal orientations (σ_ϕ) and median wobbling area (Ω_{med}), despite looking quite similar in the standard SMLM image. These observations suggest that one of the limbs could be a new growth from the main stem of the amyloid fibril, and the other is a

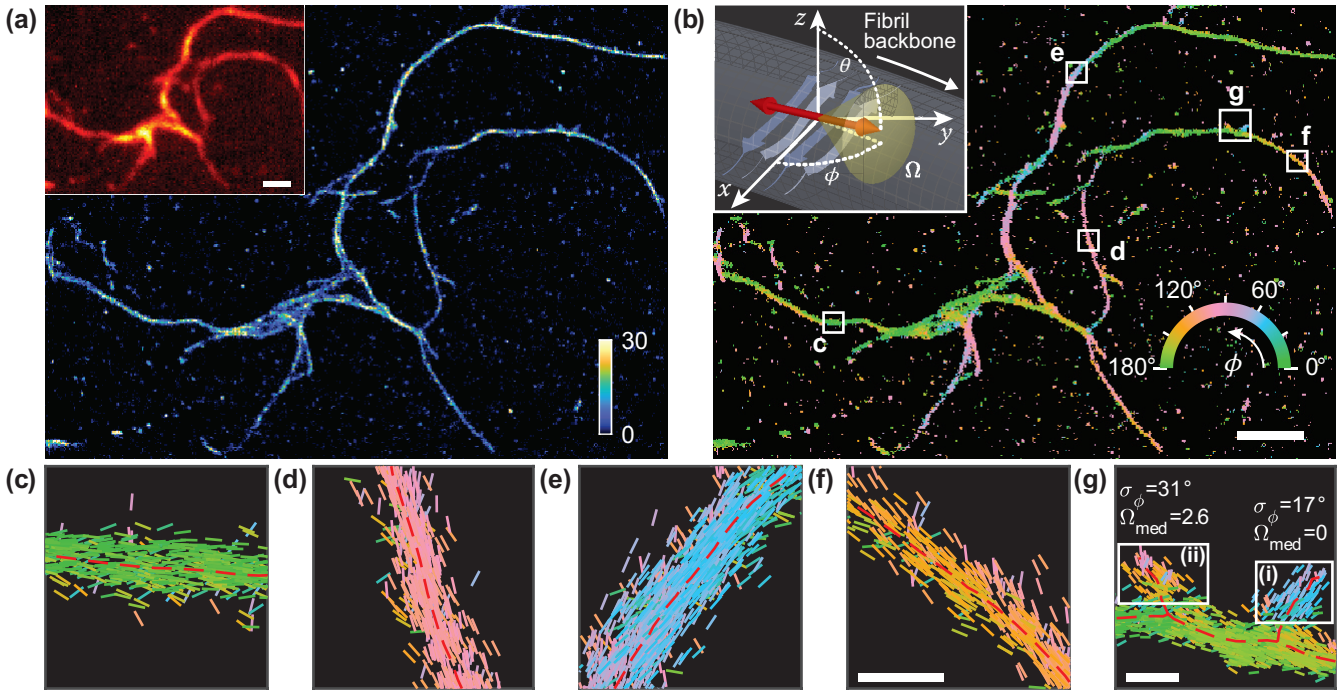

FIG. 2. Transient amyloid binding (TAB) SMLM and SMOLM images acquired using Nile red (NR). (a) SMLM image of a network of Aβ42 fibrils. Color bar: localizations per bin (20×20 nm^2). Inset: diffraction-limited image. (b) TAB SMOLM image, color-coded according to the mean azimuthal (ϕ) orientation of NR molecules measured within each bin. Inset: Main binding mode of NR to β-sheets, i.e., dipole moments aligned mostly parallel to the long axis of a fibril (its backbone). (c-g) All individual orientation measurements localized along fibril backbones within the white boxes in (b). The lines are oriented and color-coded according to the direction of the estimated ϕ angle. Red dashed lines depict fibril backbones estimated from the SMLM image. Scale bars: (a,b) 1 µm, (f,g) 100 nm.

separate aggregate deposit adsorbed to the fibril. Therefore, the orientations of NR molecules reveal structural details of amyloid aggregates that cannot be detected by standard SMLM.

To further correlate the orientations of single-molecule probes with the structural organization of amyloid aggregates, we imaged an amyloid aggregate containing obvious fibril bundles (Fig. 3(a)). The intertwined structures are evidenced by their branching architecture and their at least twice larger width (purple) compared to thinner structures (green) in the field of view (Fig. S14). We observed NR to be mostly parallel to the backbone (Figs. 3(b)(i), 3(c)(i) and Movie S2) of the thin fibrils, whereas thicker bundles cause NR to bind with relatively disordered ϕ angles (Figs. 3(b)(ii), 3(c)(ii) and Movie S2). Since NR binds to specific grooves within the stacked β-sheet aggregate, these orientation measurements indicate highly aligned β-sheets within the thin fibrils. We consistently observed similarly disordered ϕ orientations of NR on thicker aggregates compared to thinner structures (Figs. S17 and S18). These disordered ϕ angles show that the β-sheets within bundles of amyloid fibrils exhibit a complex and heterogeneous architecture.

We note that the wobbling area Ω, which can indicate the binding strength between NR and the surrounding β-sheet grooves, also exhibits obvious differences between the two regions. We observed small Ω values on the thin fibril (Figs. 3(d)(i), S15(a) and S15(b)) and large wobbling on the fibril bundle (Figs. 3(d)(ii), S15(a) and S15(c)) that represent tight and loose binding of NR molecules to each local region, respectively. From these measurements, we speculate that fibril bundling not only produces relatively disordered β-sheet orientations due to the entwining of multiple fibers but also increases dramatically the local density of binding sites for NR, thereby causing large NR wobbling during a single fluorescence burst. Note that we did not observe significantly different burst times for NR on thin fibers ($\tau_{\rm on} = 13$ ms in Fig. 3(b)(i)) versus disordered fibrillar bundles ($\tau_{\rm on} =$ 11 ms in Fig. 3(b)(ii)).

Interestingly, the local structural heterogeneity in amyloid fibrils detected by SMOLM is not always associated with thicker fibrils in standard SMLM. We observed similar disordered ϕ values and large Ω estimates from a fibril in another field of view (Fig 3(e)). Although the two fibril strands have similar thickness, the estimated ϕ and Ω distributions show noticeable differences (Fig. 3(f)-3(h)). These measurements suggest the fibril in Fig. 3(f)(ii) may consist of more disorganized assemblies of β-sheets compared to that of Fig. 3(f)(i). Similar to the small aggre-

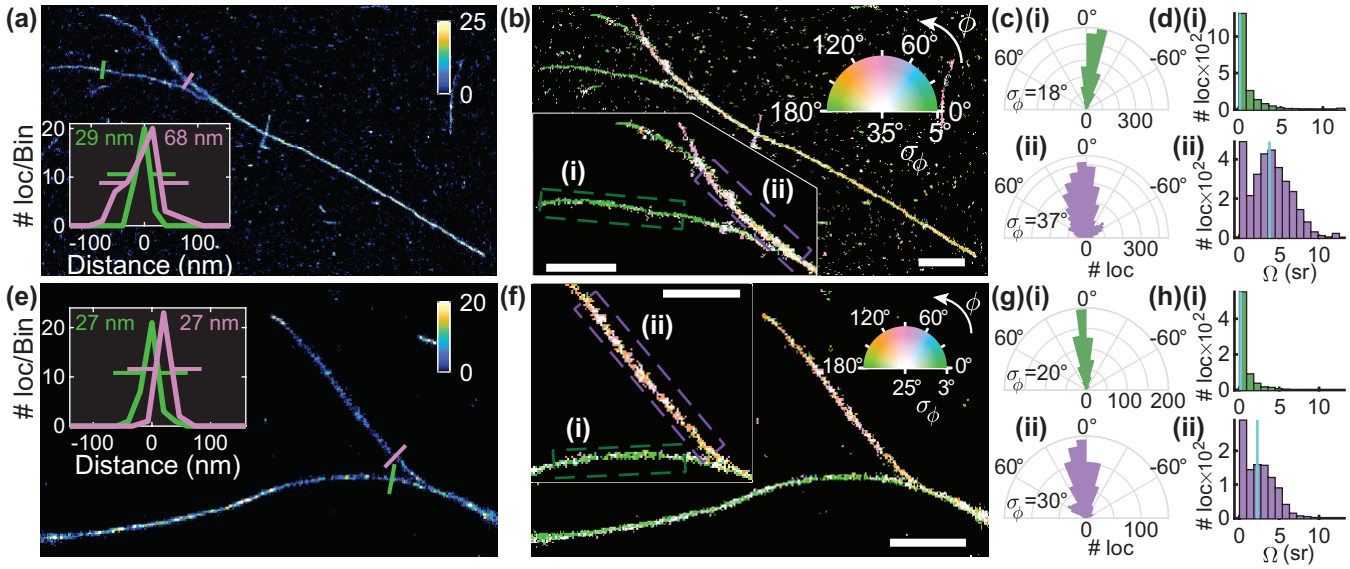

FIG. 3. Structural heterogeneity of Aβ42 fibrils revealed by TAB SMOLM imaging. (a) SMLM image of fibril bundles. Color bar: localizations per bin (20×20 nm^2). Inset: fibril cross-sections at the locations denoted by green and purple lines with measured full-width at half-maximum (FWHM) thicknesses. (b) TAB SMOLM image corresponding to (a), color-coded according to the mean (ϕ) and standard deviation (σ_ϕ) of the azimuthal orientation measured within each bin. Inset: zoomed (i) thin and (ii) thick fibril regions isolated from background structures. (c) Histograms of measured azimuthal orientations relative to the fibril backbone within the regions denoted in (b), showing standard deviations (σ_ϕ) of (i) 18° and (ii) 37°. (d) Measured wobbling areas (Ω) corresponding to the localizations in (c), yielding median wobbling areas (Ω_{med}, cyan) of (i) 0.14 sr and (ii) 3.77 sr. (e-h) TAB SMLM and SMOLM images of another fibril field of view, as in (a-d). Although fibril regions (i) and (ii) in the inset of (f) show little difference in apparent width, the measured orientation distributions contain significant differences. The standard deviations of azimuthal angles σ_ϕ are (i) 20° vs (ii) 30°, and the median wobbling areas (Ω_{med}, cyan) are (i) 0.14 sr vs (ii) 2.25 sr. Scale bars: 1 μm.

gates shown in Fig. 2(g), the local heterogeneity cannot be resolved by conventional SMLM.

CONCLUSION

Here, we propose and characterize a new variance upper bound (VUB) for efficiently quantifying the sensitivity of any PSF for measuring the orientation and wobble of dipole-like emitters. Since the orientational second moment vector $\boldsymbol{m}$ is six dimensional, VUB greatly accelerates the comparison of various PSFs for any specific imaging scenario. While VUB overestimates the mean variance of an orientation measurement by 36%, computing the VUB is ~1000 times faster than evaluating the average CRB across orientation space with sufficient sampling. Using VUB, we discover that imaging dipoles near a refractive index interface enables the simple polarized standard PSF to robustly measure orientational dynamics, particularly within the xy plane, that cannot be detected in matched media.

Using the polarized standard PSF, our SMOLM images of amyloid aggregates confirm that the main binding orientation of NR is mostly parallel to the long axis of the fibrils. In cases where multiple fibrils are intertwined, TAB SMOLM detects heterogeneities in the stacking of β-sheets via larger variations in NR orientations and increased wobbling angles. In particular, SMOLM detects structural disorder within the fibrillar network cannot be resolved by simple SMLM analysis of fibrillar width or NR binding time.

Simultaneous imaging of single-molecule positions and orientations in SMOLM allows scientists to quantify local structural features on a nanometer scale without ensemble averaging. In particular, measuring the full spatial configuration (i.e., positions and orientations) of molecules provides unprecedented insight into dynamical molecular activities that aren't revealed with location information alone. The computational advantages afforded by VUB could enable PSFs for SMOLM to be optimized in real-time to attain the best-possible measurement precision within the specific sample of interest. In the future, SMOLM combined with transient binding of amyloid-sensitive fluorogenic molecules could become a powerful tool for visualizing the structural dynamics of amyloid aggregation with nanoscale resolution over periods of hours to days [11]. SMOLM imaging of structural heterogeneity across and within individual aggregates may reveal underlying mechanisms of aggregation and depolymerization and perhaps provide links between structure and toxicity necessary for developing effective

therapeutics against amyloidosis.

Acknowledgments

Research reported in this publication was supported by the National Science Foundation under grant number ECCS-1653777 and by the National Institute of General Medical Sciences of the National Institutes of Health under grant number R35GM124858. The authors thank Jan Bieschke, Jin Lu, and Kevin Spehar for helpful suggestions and comments.

† These authors contributed equally to this work

* mdlew@wustl.edu

[1] H. Sosa, E. J. Peterman, W. E. Moerner, and L. S. Goldstein, Nature Structural Biology **8**, 540 (2001).

[2] E. J. Peterman, H. Sosa, L. S. Goldstein, and W. Moerner, Biophysical Journal **81**, 2851 (2001).

[3] L. G. Lippert, T. Dadosh, J. A. Hadden, V. Karnawat, B. T. Diroll, C. B. Murray, E. L. F. Holzbaur, K. Schulten, S. L. Reck-Peterson, and Y. E. Goldman, Proceedings of the National Academy of Sciences **114**, E4564 (2017).

[4] T. Ha, J. Glass, T. Enderle, D. S. Chemla, and S. Weiss, Physical Review Letters **80**, 2093 (1998).

[5] A. S. Backer, A. S. Biebricher, G. A. King, G. J. L. Wuite, I. Heller, and E. J. G. Peterman, Science Advances **5**, eaav1083 (2019).

[6] B. Dong, Y. Pei, N. Mansour, X. Lu, K. Yang, W. Huang, and N. Fang, Nature Communications **10**, 4815 (2019).

[7] R. J. Ober, S. Ram, and E. S. Ward, Biophysical journal **86**, 1185 (2004).

[8] G. Grover, K. DeLuca, S. Quirin, J. DeLuca, and R. Piestun, Optics Express **20**, 26681 (2012).

[9] Y. Shechtman, S. J. Sahl, A. S. Backer, and W. E. Moerner, Physical Review Letters **113**, 1 (2014).

[10] D. Patra, I. Gregor, and J. Enderlein, J. Phys. Chem. A **108**, 6836 (2004).

[11] K. Spehar, T. Ding, Y. Sun, N. Kedia, J. Lu, G. R. Nahass, M. D. Lew, and J. Bieschke, ChemBioChem **19**, 1944 (2018).

[12] H. Mazidi, E. S. King, O. Zhang, A. Nehorai, and M. D. Lew, in *IEEE 16th International Symposium on Biomedical Imaging (ISBI)*, 325–329 (2019).

[13] H. Mazidi, T. Ding, and M. D. Lew, `https://github.com/Lew-Lab/RoSE-O`.

[14] D. L. Sackett and J. Wolff, Analytical Biochemistry **167**, 228 (1987).

[15] A. Sharonov and R. M. Hochstrasser, Proceedings of the National Academy of Sciences **103**, 18911 (2006).

[16] L. Novotny and B. Hecht, *Principles of Nano-Optics* (Cambridge University Press, 2006).

[17] A. S. Backer and W. Moerner, The Journal of Physical Chemistry B **118**, 8313 (2014).

[18] A. S. Backer and W. Moerner, Optics express **23**, 4255 (2015).

[19] M. Böhmer and J. Enderlein, JOSA B **20**, 554 (2003).

[20] M. A. Lieb, J. M. Zavislan, and L. Novotny, JOSA B **21**, 1210 (2004).

[21] A. S. Backer, M. P. Backlund, A. R. von Diezmann, S. J. Sahl, and W. Moerner, Applied physics letters **104**, 193701 (2014).

[22] O. Zhang, J. Lu, T. Ding, and M. D. Lew, Applied physics letters **113**, 031103 (2018).

[23] A. S. Backer, M. P. Backlund, M. D. Lew, and W. E. Moerner, Optics letters **38**, 1521 (2013).

[24] E. Cohen, J. Bieschke, R. M. Perciavalle, J. W. Kelly, and A. Dillin, Science **313**, 1604 (2006).

[25] M. Serra-Batiste, M. Ninot-Pedrosa, M. Bayoumi, M. Gairí, G. Maglia, and N. Carulla, Proceedings of the National Academy of Sciences **113**, 10866 (2016).

[26] L. M. Young, L.-H. Tu, D. P. Raleigh, A. E. Ashcroft, and S. E. Radford, Chemical Science **8**, 5030 (2017).

[27] M. G. Iadanza, M. P. Jackson, E. W. Hewitt, N. A. Ranson, and S. E. Radford, Nature Reviews Molecular Cell Biology **19**, 755 (2018).

[28] G. Fusco, S. W. Chen, P. T. F. Williamson, R. Cascella, M. Perni, J. A. Jarvis, C. Cecchi, M. Vendruscolo, F. Chiti, N. Cremades, L. Ying, C. M. Dobson, and A. De Simone, Science **358**, 1440 (2017).

[29] J.-E. Lee, J. C. Sang, M. Rodrigues, A. R. Carr, M. H. Horrocks, S. De, M. N. Bongiovanni, P. Flagmeier, C. M. Dobson, D. J. Wales, S. F. Lee, and D. Klenerman, Nano Letters **18**, 7494 (2018).

[30] J. A. Varela, M. Rodrigues, S. De, P. Flagmeier, S. Gandhi, C. M. Dobson, D. Klenerman, and S. F. Lee, Angewandte Chemie International Edition **57**, 4886 (2018).

[31] H. A. Shaban, C. A. Valades-Cruz, J. Savatier, and S. Brasselet, Scientific Reports **7**, 12482 (2017).

[32] M. Biancalana and S. Koide, Biochimica et Biophysica Acta - Proteins and Proteomics **1804**, 1405 (2010).